Simulation and Measurement of Local Potentials of Modified Commercial Cylindrical Cells - Part I: Cell Preparation and Measurements

P. Osswald[a,*], S. Erhard[b], J. Wilhelm[b], H. Hoster[c], A. Jossen[b]

[a]*TUM CREATE Ltd., Singapore*
[b]*Institute for Electrical Energy Storage Technology (EES), Technische Universität München, Munich*
[c]*Energy Lancaster, Lancaster University, Lancaster*

Abstract

This work presents a modification approach and first measurements of commercial cylindrical Li-ion cells with local potential probes and internal temperature sensor. Local potential measurements at low currents show a non-uniform potential distribution along the electrode, dominated by the open circuit voltage (OCV) of the negative electrode. For higher currents, the overpotential along the current collector becomes dominant and instead of a corrugated potential distribution, a strong current depended voltage gradient is measured, suggesting a highly non-uniform state of charge (SOC) distribution with increasing distance to the current tab. After discharge, a fast potential equalization takes place and no potential difference between the single electrode sections can be measured after 12 min, even though the overall cell voltage relaxation has not reached an equilibrium state yet. The presented modification approach combines the advantages of high quality industrial manufactured cells as uniform coating thickness and density with the advantages of special tailor made cells for in-situ measurements. Due to the low impact of the modification and its long-term stability, detailed measurements at different sections of the electrode become available.

Keywords: internal temperature, current density distribution, local state of charge (SOC) inhomogeneities, local potential, commercial cell modification

1. Introduction

Li-ion cells show continuing commercial success as power source in the consumer application market. High energy density, safety and reliability make them the secondary battery of choice for portable electronics such as mobile phones and laptop computers [1, 2]. In recent years, Li-ion batteries increasingly find application in the field of full and hybrid electric vehicles (FEVs/ HEVs)which demand for power optimized large capacity batteries [3]. Upscaling established Li-ion technology with capacities of up to 100 Ah, while retaining the energy density and reliability of smaller systems is a continuing technological challenge [source].

Designing an effective large format battery is supported by simulation tools of varying degree of complexity, ranging from early 1-Dimensional models utilizing porous electrode theory by Newman et al. [4], over analytical calculations [5, 6] to more recent multi-scale multi-dimensional model frameworks combining various approaches [7, 8, 9]. These models predict in detail the spatial distribution and time evolution of cell parameters such as potential, current, state of charge (SOC) and temperature. Yet, little spatially resolved experimental data is available for model validation. Inhomogeneities in the degree of lithiation have been investigated by means of neutron diffraction [10], calorimetry [11], X-ray micro-diffraction (μXRD) [12] and Raman spectroscopy [13]. These methods typically rely on custom small scale in-situ cells or ex-situ measurements on materials from disassembled cells. Neutron diffraction and topography allow for in-situ measurement of the degree of lithiation, i.e., the local SOC in commercial cells due to the high penetration depth compared to X-rays or Raman spectroscopy. But the resulting SOC distribution is an average of multiple layers, depending on the battery geometry and electrode positions [14].

Spatially resolved temperature data has been gathered by means of applying multiple external [15, 16] and internal sensors [17, 18, 19, 20] and by measuring the thermal radiation.

Due to its increasing application in EVs, large format pouch cells are of particular interest. Ng. et al. built a multi-layer electrode pouch cell and found inhomogeneities in the electrode material perpendicular to the current collectors. Zhang et. al. built a large format pouch cell with a segmented cathode and a long, z-folded anode and measured the current through each segment along with the resulting SOC inhomogeneities at several operation scenarios [21, 22]. Presumably, data from custom cells are scarce as the requirements to achieve similar quality as consumer grade cells are hard to fulfill.

*Corresponding author
Email address: pjo@tum.de (P. Osswald)

High power cylindrical cells face the challenge to support very high discharge rates while generating high temperatures due to their long electrodes. To the best knowledge of the authors of this work, current and potential distribution data is not available for this type of cell.

In this work, commercial cylindrical cells are modified to allow for in-situ local potential and internal temperature measurements. We evaluate the quality and stability of the modified cells through impedance measurements and long term cycling. First measurements of spatially resolved potential data at various discharge scenarios and during relaxation are presented.

2. Experimental work

Cell modification procedure - The cells used in this work for modification are commercially available 26650 cells with a capacity of 2.5 Ah and an average discharge voltage of 3.3 V. Lithium iron phosphate (LFP) is used for the cathode, graphite for the anode, whereas the active material is double coated on the current collectors with a thickness of 70 μm for the cathode and 35 μm for the anode respectively. The aluminum current collector on the cathode has a thickness of 20 μm, the copper current collector on the anode side 13 μm respectively. As common in commercial cells, the anode width of 5.75 cm overlaps the cathode by 0.1 cm on each side. The cathode has an overall length of 169 cm, the anode 175 cm and each electrode has four almost equidistant current tabs. Figure 1 a) gives an overview of the cell dimensions and tab positions.

The tab distances lead to symmetrical tab alignment on both electrodes in order to facilitate the spot-welding with an additional layer of the respective current collector material to the top and bottom cap of the cell (Figure 2). Figure 1 b) and c) illustrates the two different modes of operation before and after modification. The four current tabs in the unmodified cell are connected and the cell voltage is measured at the terminal. The separation of the tabs in the modified cell allows the voltage measurement a four different positions of the electrode while in this work only the outermost tab is used to apply a current.

For safe handling during the cell modification, all cells were discharged with a current of 0.2C (1C = 2.5 A) to the cut-off voltage of 2 V and opened in an argon filled glove box. The modification is applied on the negative and the positive electrode, starting with the positive electrode as it is connected to the cell housing. The caps were removed and the four current tabs of the electrodes, which are welded onto the caps, were separated.

Nickel tabs (3 cm length, 4 mm width, 80 μm thickness) were spot-welded onto the aluminum tabs on the cathode and on the copper tabs at the anode side. A MSK-310 compact AC pulse spot welder from MTI Corporation was modified to allow operation inside the glove box. After extending the current tabs, the cells were sealed with self-made polymer caps and epoxy glue as schematically shown in Figure 3. Each polymer cap
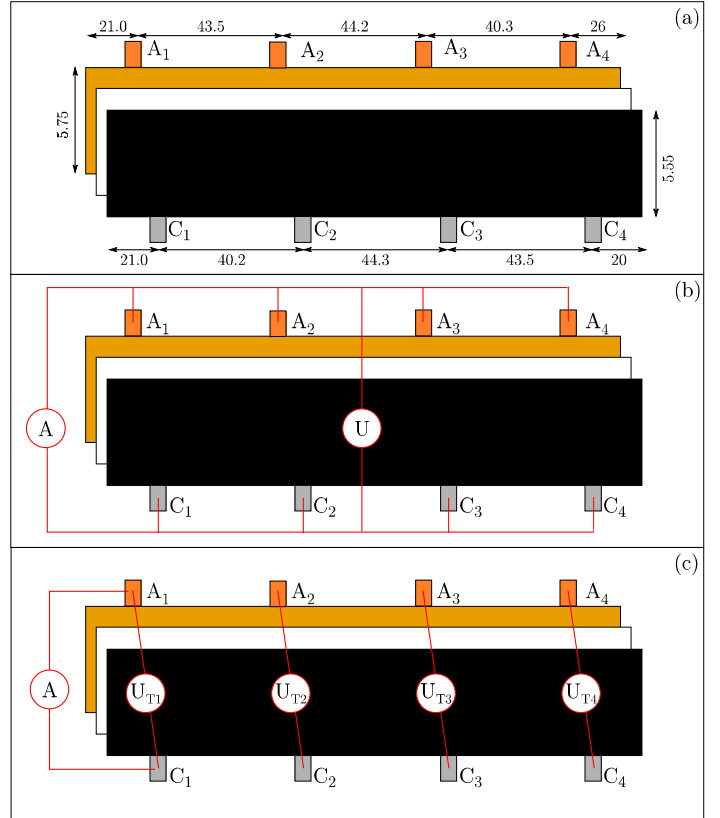

Figure 1: Schematic drawing of the rolled out modified experimental cell with the over all dimensions of the cell (a). $C_1 - C_4$ denote the positive electrode tabs, $A_1 - A_4$ the negative current tabs. C_1 and A_1 are the outermost tabs of the cell.

has four feedthroughs for the current tabs; the cap on the positive electrode has an additional feed-through for a temperature sensor. The thermocouple is housed in the center of the steel rod in the middle of the cell.

Experimental set-up and test procedure - Before and after the cell modification, each cell received a performance check-up at different discharge currents (0.5C, 1C, 2C) with 2 h relaxation period in between and a constant current constant voltage (CC-CV) charging protocol (0.2C, 3.6 V CV, 0.01C cut-off). All cycling experiments were conducted at ambient temperature at 22 °C with a BaSyTec CTS to cycle the cells. In addition, an Agilent 39720 with a 20 channel multiplexer was connected for supplementary voltage and temperature measurements. Before modification, the cells are contacted via a spring loaded kelvin probe holder. After modification, 2 mm banana plugs are soldered on the nickel tabs. All temperature measurements, inside as well as outside, were conducted with T-type thermocouples (class A) with an accuracy of ±0.5 K from Labfacility Ltd. The conductor thickness was 200 μm for outside measurements and 76 μm for in-cell measurements. The tip of the thermocouples mounted inside the cell were insulated with Apiezon© to avoid electrical contact or contamination.
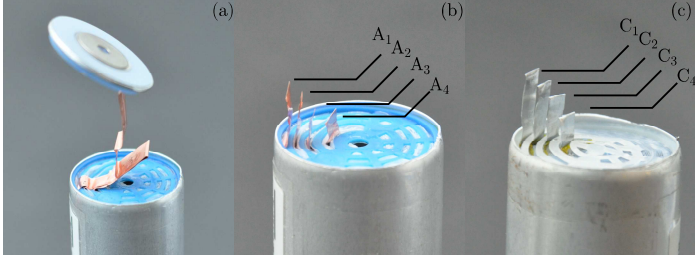
Figure 2: Experimental cell, opened on the negative electrode (a) and with separated current tabs on the negative (b) and positive electrode (c)
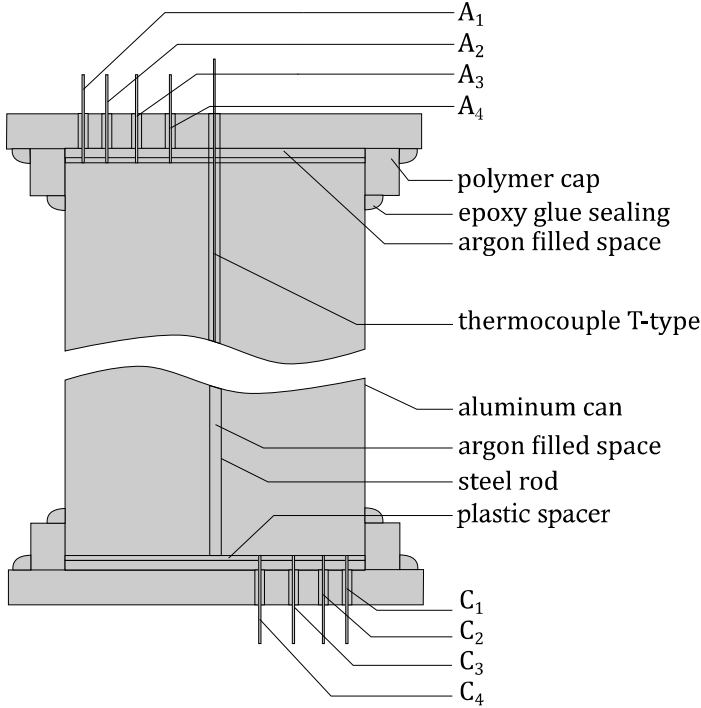

Figure 3: Schematic drawing of the experimental cell after modification, terminal T_1 ($C_1 - A_1$), is used for cycling the cell while the terminals T_2, T_3 and T_4 are used for voltage measurements only

3. Results and Discussion

Stability of Experimental cell - To allow the comparison of the performance of a modified cell with its original state, it had to be guaranteed that the performance of the cell has not been affected by the modification. As the cell undergoes different handling steps, including opening and resealing the cell, certain error sources are possible. Contamination or loss of a significant amount of electrolyte due to evaporation would result in immediate side reactions or performance loss and capacity decrease. A non-proper sealing would lead to the ingress of water and oxygen into the cell, causing a constant loss of capacity within a short time. Different pre-measurements were done to validate the cell performance before and after modification.

Cell resistance and impedance - According to the cell data sheet, a new cell has a typical impedance of 6 mΩ at 1000 Hz. The impedance of a modified cell can be described by a more complex impedance network consisting of multiple elements as shown in Figure 4.
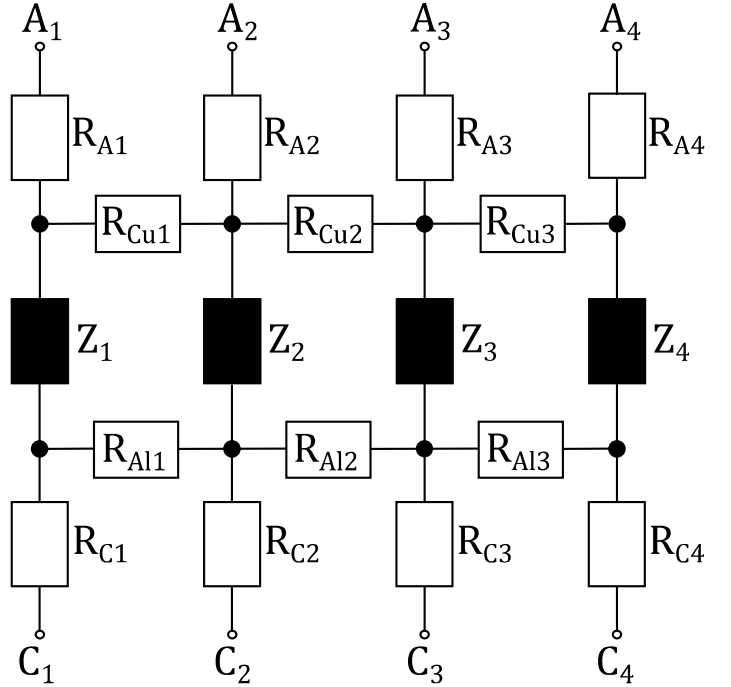

Figure 4: Schematic multi-element impedance matrix for a modified cell

The terminal T_n describes the impedance or voltage between the current tab of the cathode C_n and the restrictive anode A_n whereas $1 \leq n \leq 4$ denotes the number of the current terminal, with $n = 1$ being the outermost current terminal (refer to Figure 3). It consists of the cell impedance Z_n as well as the resistances of the nickel tabs and the new welding spots $R_{C,n}$ and $R_{A,n}$.

$R_{Al,n}$ and $R_{Cu,n}$ ($1 \leq n \leq 4$) represent the resistances between each tab and depend on the current collector geometry with 24.62 mΩm^{-1} for the positive and 23.07 mΩm^{-1} for the negative electrode respectively. $R_{C1} - R_{C4}$ and $R_{A1} - R_{A4}$ represent the calculated resistance values of the single nickel tab and corresponding welding spot. The measured and averaged impedances of a modified cell are summarized in Table 1.

All measurements were conducted with several iterations with a Hioki BT3562 Battery Impedance Tester at 1 kHz. The resistances measured at the terminals range from 19.76 mΩ to 26.54 mΩ, caused by the non-uniform contact resistance at the welded spots. To identify the contact resistance of each weld spot, the resistances $R_{C1} - R_{C4}$ and $R_{A1} - R_{A4}$ listed in Table 1 were calculated. For this work, only T_1 was used as current tab and $T_2 - T_4$ were used for voltage measurement.

Electrical and thermal characteristics - Figure 5 depicts the voltage characteristics at discharge currents of 0.5C, 1C and 2C before and after the cell modification.

Table 1: Measured impedance T_n between the cell terminals, the measured resistance between the current tabs and calculated resistance of the nickel tabs and the respective welding spot R_{Cn} and R_{An}

	mΩ		mΩ
T_1	26.54	T_3	24.84
T_2	23.30	T_4	19.76
C_1 - C_2	21.59	A_1 - A_2	33.73
C_2 - C_3	24.51	A_2 - A_3	30.07
C_3 - C_4	23.43	A_3 - A_4	25.68
R_{C1}	4.21	R_{A1}	12.68
R_{C2}	7.48	R_{A2}	11.02
R_{C3}	6.11	R_{A3}	8.86
R_{C4}	6.61	R_{A4}	7.53

Table 2: Performance of an experimental cell before and after modification

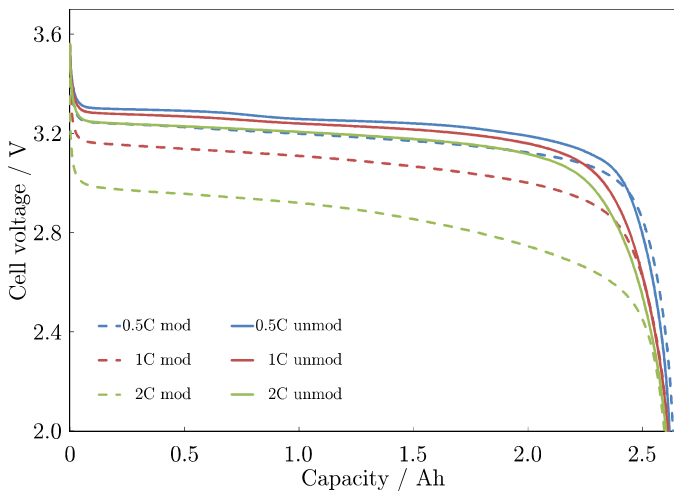| C-rate	0.5C	1C	2C
C_{unmod}/Ah	2.6174	2.6101	2.6021
C_{mod}/Ah	2.6321	2.6120	2.5949
$\Delta C/\%$ $_{C_{unmod} = 100\%}$	0.56	0.07	-0.28
$\bar{U}_{unmod}/V$	3.1335	3.0504	2.9523
$\bar{U}_{mod}/V$	3.0815	2.9498	2.7599
$\Delta \bar{U}/mV$	52.0	100.6	192.4

Figure 5: Discharge performance of the cells before (solid) and after (dashed) the modification at discharge rates of 0.5C, 1C and 2C

clear illustration in Figure 6, the data for 1C and for 2C were offset by 1 K and 2 K respectively.
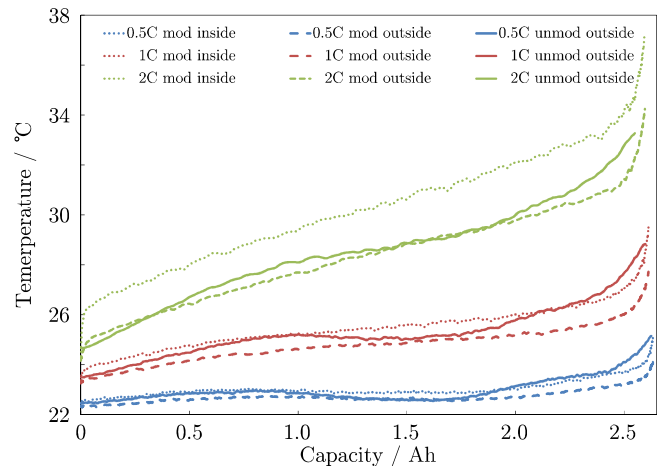

Figure 6: Temperature profiles of the cells before and after the modification at a discharge rate of 0.5C, 1C and 2C, measured on the cell surface as well as the cell core of the modified cell. The measured data at 1C was offset by 1 K and the measured data at 2C by 2 K for clearer illustration

The high power capability of the cell provided a stable capacity C_{unmod} with increasing current of 2.6174 Ah at 0.5C, decreasing by 0.59% to 2.6021 Ah at 2C. Due to the higher overpotential at higher currents, the average discharge voltage $\bar{U}_{unmod}$ decreased from 3.1335 V to 2.9523 V. After modification, the current is applied via at T_1 (C_1-A_1) for cycling. The capacity C_{mod} was 2.6321 Ah at 0.5C and 2.5949 Ah at 2C, resulting in a capacity increase of 0.56% at 0.5C and a capacity decrease of 0.28% at 2C compared to its unmodified state. This minor increase of capacity for lower currents could be assigned to a slight increase of the ambient temperature during or a longer relaxation time before testing. Cycling the cell only via terminal T_1 leads to a larger potential drop as in the unmodified cell and is superimposed by the added contact resistances from the nickel tabs and the corresponding welding spots. Compared to the average discharge voltage $\bar{U}_{unmod}$, $\bar{U}_{mod}$ decreases nearly proportional to the applied current by $52\,\mathrm{mV}, 101\,\mathrm{mV}$ and $192.4\,\mathrm{mV}$ as specified in Table 2.

The temperature during discharge suggests a change of the thermal properties of the modified cells (Figure 6). For

The temperature of an unmodified cell, measured outside at the middle of the cell, ranges from 22.5 °C to 25 °C for 0.5C and increases to 28 °C for 1C and 31.2 °C for 2C respectively. The self-cooling between 1 Ah and 2 Ah due to the entropic effects in the graphite anode [23, 20] is visible for lower currents up to 1C and vanishes for 2C. In the modified cell, this self-cooling effect is less dominant and nearly disappears at currents above 1C. This change can be attributed to the modification process, as the heat capacity was increased due to additional parts such as polymer caps the on both sides of the modified cell. In addition, the current tabs, prior welded to the metal caps, were separated, resulting in a lower thermal conductivity from the inside to the outside of the cell.

Long term cycling - To verify the stability of the modified cell and to compare the ageing behaviour between the modified and unmodified cells, long-term cycling experiments at ambient temperature were conducted. Figure 7 represents the capacity fade of one modified cell and two unmodified cells after 480 full cycles.

In contrast to the characterization measurements, for the long-term cycling the four nickel tabs on each electrode were interconnected and the cells were charged with
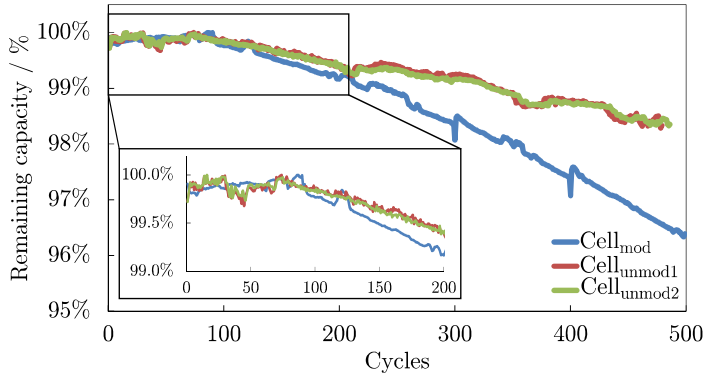
Figure 7: Long term performance of one modified and two new cells after 200 and 480 cycles respectively. The cells were cycled between 0 and 100% SOC with a 1C rate at ambient temperature

Figure 8: Discharge voltage U_{Tn} for a modified cell for 0.1C (a) and 2C (b) measured at the terminals T_n ($1 \leq n \leq 4$)

2.5 A, equivalent to 1C for 60 min. If the cut-off voltage of 3.6 V was reached before 60 min, the remaining time was conducted as CV charging. As discharge procedure, a 1C current was applied until the cell reaches cut-off voltage at 2 V. The cell capacities show only very small variations during the first cycles with a difference of 0.23 % after 200 cycles. Afterwards, the relative capacity loss for the unmodified cells continues linearly while the capacity loss of the modified cell increases slightly. After 480 cycles, the unmodified cells lost 1.67% and 1.65% of the initial capacity, the modified cell 3.52% respectively. To further investigate the durability of the modified cell, additional 520 cycles were applied. After 1000 cycles, the modified cell reveals a capacity loss of 10.62%. The cells show a very stable long-term performance, indicating that only minor side reaction due to ingress of moisture or oxygen after the modification occurred.

3.1. Local Potential Measurements

Local potential measurements - To investigate the local potential, the cell was discharged at different C-rates (0.1C, 0.5C, 1C, 2C), applying current to terminal T_1 while the terminals T_2, T_3 and T_4 are used for potential measurements. In Figure 8 the voltage U_{Tn} of the different tabs is shown for 0.1C (a) and 2C (b). For low currents, the potential at all tabs remain contiguous. For higher currents, the potential difference increases towards lower SOC.

Subtracting the voltage $U_{T,2}$, $U_{T,3}$ and $U_{T,4}$ from the current carrying tab U_{T1} discloses a non-constant potential difference between the individual positions as shown in Figure 9. The difference between the tab voltages could give implications to local current density distribution and superimposed redistribution of charge. For low currents as 0.1C, the potential difference at 0% and 100% SOC is constant, but distinct local minima and maxima at different SOCs in between are measured. The increase in amplitude for increasing distance to T_1. At 0.1C, a transient behavior can be observed within the first 5% SOC during discharge. After that, the initial potential drop along the current collector stabilizes and increases from 13.6 mV
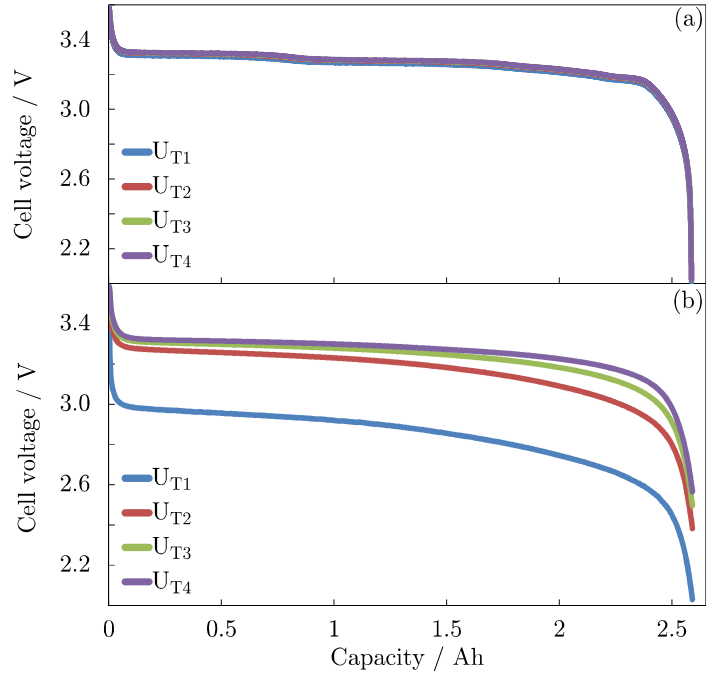
between U_{T1} and U_{T2} to 16.1 mV between U_{T1} and U_{T3} and 17.3 mV between U_{T1} and U_{T4} as shown in Figure 9 a). For higher currents at 0.5C (b), the extrema attenuate and are superimposed by a negative slope. At 2C (c), the extrema vanish, except a small local maxima at 2.55 Ah.

The additional voltage difference between U_{T1} and U_{T4} of 4 mV at the local minimum A in Fig 9 a) can be attributed to a difference in the degree of lithiation along the electrode. LFP features a constant potential vs. Li/Li^+ in a wide SOC range [24, 25]. In contrast to LFP, graphite is characterized by different voltage plateaus and steps, depending on the degree of lithiation [26, 27]. These characteristics are measurable in the experimental cell and become more pronounced at lower currents. Figure 10 shows the measured voltage of graphite versus Li/Li^+ in a half-cell during lithiathion with 0.05C with an inset magnifying the transition from stage-1 (LiC_6) to stage-2 (LiC_{12}).

The measured voltage difference ΔU_{T1-T4} indicates a different lithium concentration of the anode at the respective positions as highlighted. As the current is low, only a small additional overpotential due to diffusive and kinetic limitation is measured, reflected in a small but constant gradient along the whole SOC range. The potential difference ΔU_{T1-T4} returns to its initial value of 17 mV after the whole graphite electrode passes the voltage step into the the next voltage plateau, suggesting only a small SOC gradient within the cell. With increasing current, the before mentioned diffusive and kinetic limitations cause additional overpotential, dominating the measured voltage. For a current of 2C the single voltage steps in the anode are not observable and the potential difference ΔU_{T1-T4} in-
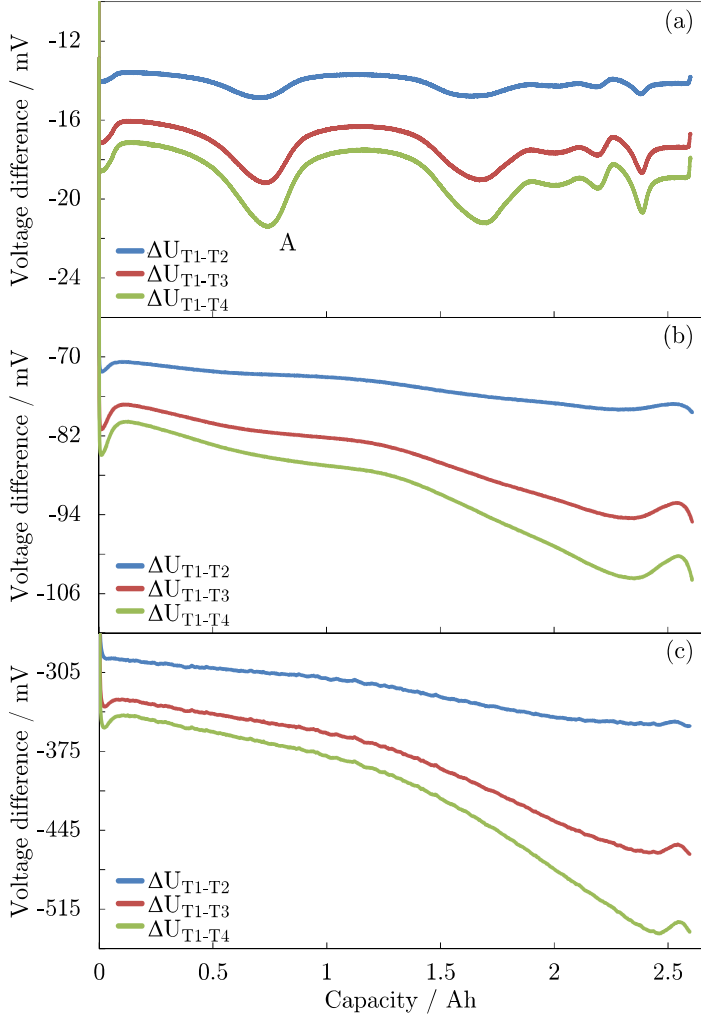
Figure 9: Potential difference ΔU_{T1-T2}, ΔU_{T1-T3} and ΔU_{T1-T4} for 0.1C (a), 0.5C (b) and 2C (c)
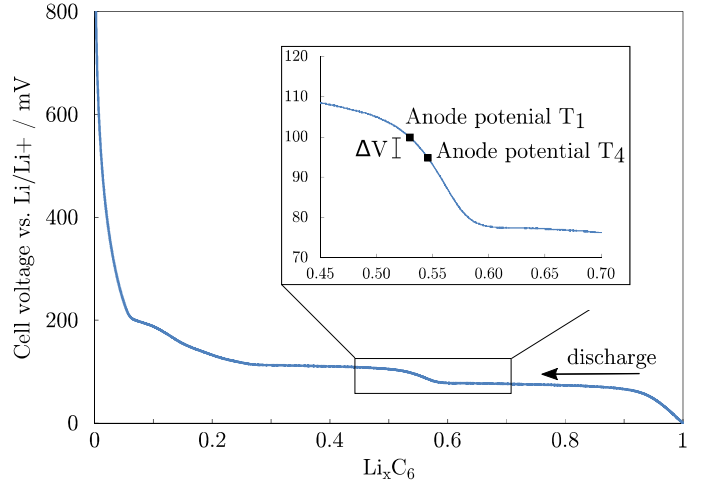

Figure 10: Exemplary half-cell voltage of graphite vs. Li/Li^+

trode material as analyzed by Bloom et. al. [28, 29, 30]. As described before, LFP does not have a phase change in the respective SOC range as it rather reveals a phase-separating behavior. If all extrema occur nearly at the same time as seen in Figure 11 a), a simultaneous phase change along the whole electrode can be expected, suggesting a homogenous SOC distribution along the electrodes. With increasing current (e.g. 0.5C Figure 11 b)), the phase changes are shifted along their position on the electrode, indicating an increasing non-uniformity in the SOC distribution with greater distance to the current tab. Once the current exceeds a certain threshold, the different phase changes within the anode material cannot be located, resulting in a U-shaped profile with steep gradients towards high and low SOCs as pictured in Figure 11 c).

creases to a maximum value of 536 mV and 193 mV without the potential drop along the current collector respectively, indicating a steep gradient in the current density distribution along the electrodes.

Figure 11 shows the derivative with respect to time dU_n/dt of the terminal voltages U_{T1}, U_{T2}, U_{T3} and U_{T4} as presented in Figure 8 a) and b) for different C-rates. The data were recorded every 2 s for all measurements and a 15-point moving average filter was applied to reduce noise especially at low discharge rates. The voltage derivatives at the individual tab positions are very similar for 0.1C, the extrema (A,B,C) occur at the same SOC with only small derivations in the amplitude. For a current of 0.5C, the number of extrema decreases significantly and the local minimum at A occurs between 0.57 Ah and 1.07 Ah, but the local minimum C nearly vanishes. For higher currents as depicted in Figure 11 c) for 2C, all derivatives show a similar shape without extrema and steep gradients towards high and low SOCs.

For constant current discharge, extrema in the dU_n/dt curves can be interpreted as phase changes in the elec-

Voltage relaxation behavior - The cells were discharged with different C-rates (0.5C, 1C, 2C) until the cut-off voltage of 2 V was reached at the current carrying tab and the voltage relaxation behavior at the tabs was recorded every 2 s for 60 min. The voltage differences between the current terminal T_1 and the measurement terminals T_n during the relaxation period reveal a swing in the voltage relaxation behavior within the first 2 min for currents up to 1C, while it was not observed for a current of 2C (Figure 12). As the voltage range of the swing is rather small (0.5 mV), it might still occur at higher C-rate, but is superimposed by the strong voltage equalization process. The potential differences ΔU_{T1-T2}, ΔU_{T1-T3} and ΔU_{T1-T4} converge to zero within less than 12 min, not depending on the applied discharge current.

This is highlighted in Figure 13, where the derivation of voltage difference $d(\Delta U_{T1-T4})/dt$ allows a comparison of the voltage relaxation behavior for different applied discharge currents. After 12 min, all $d(\Delta U_{T1-T4})/dt$ converge to zero, indicating a fast voltage equalization between the different sections of the electrode. The inlay in
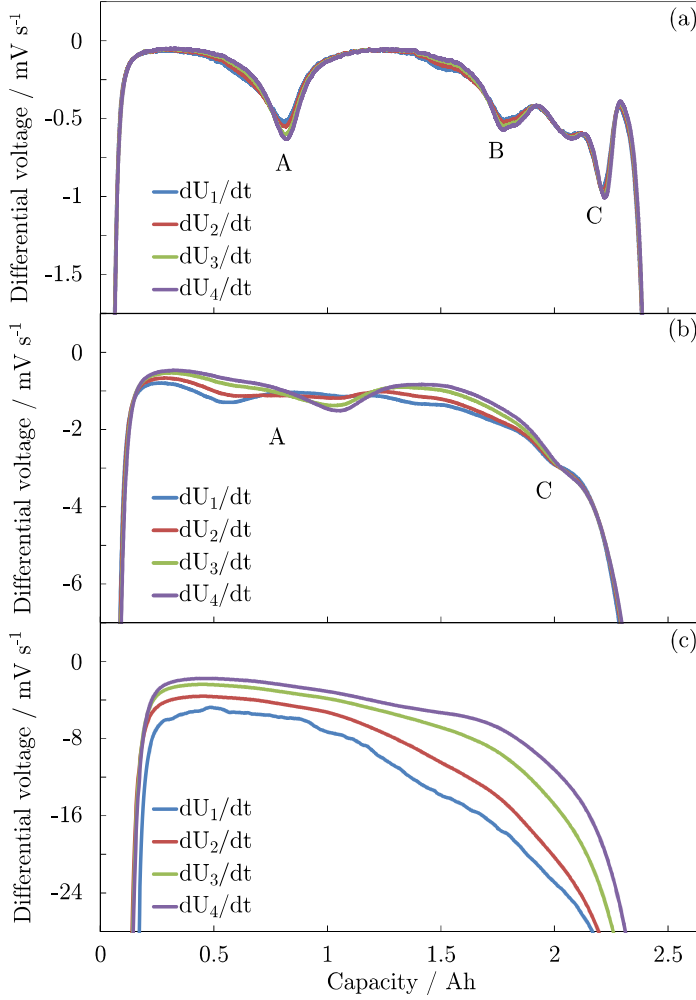
Figure 11: Differential voltage dU_n/dt for 0.1C (a), 0.5C (b) and 2C (c) at the terminals T_n ($1 \leq n \leq 4$)

Figure 13 shows the relaxation behavior of the cell after the mentioned C-rates. An ongoing voltage relaxation is observed and the cell has not reached an equilibrium state after 60 min. The electric properties of the modified cells can be exemplified by an uneven current load on four single cells in parallel. While the external equalization currents in battery packs can be measured [31], the magnitude of the internal equalization currents can only be estimated.

4. Conclusion

In this work, a new method to measure internal potentials by modification of a commercial cell is shown. The nearly equidistant tab pattern of that specific cell is utilized as feasible local measurement setup. The impact of the modification process on the cell performances has been studied. No loss of capacity was observed for measurements up to a current of 2C after modification. The increase in internal resistance and the accompanying voltage drop during discharge was attributed to the fact, that the active number of used current tabs has been decreased
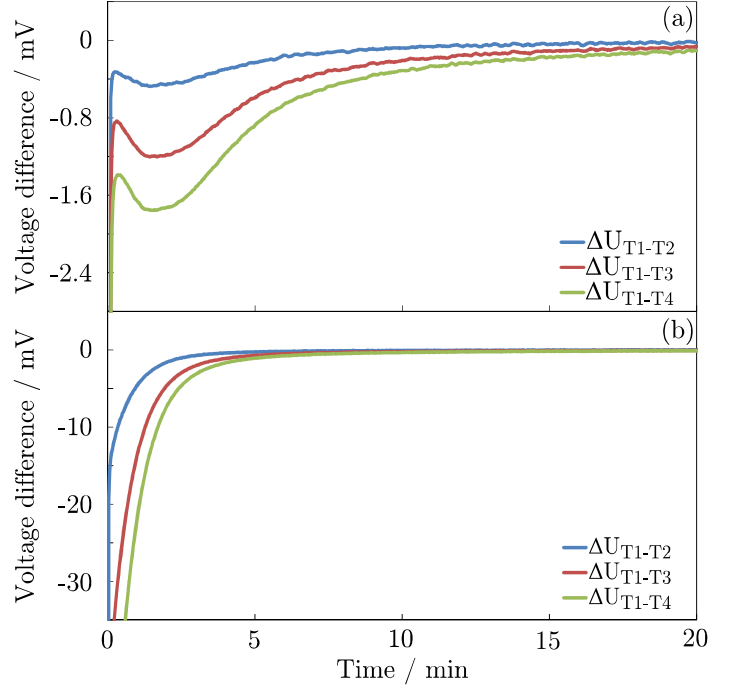

Figure 12: Potential differences ΔU_{T1-Tn} during voltage relaxation after discharging the cell at 0.5C (a) and 2C (b) until 2 V

from four to one. The modified cells show a good long-term stability with a capacity loss of 0.84% after 200 and 3.44% after 480 1C cycles respectively, indicating an additional capacity loss of 0.23 % and 1.88 % to an unmodified cell. The local potential measurements indicate a strong variation of the current density distribution. The occurring phase changes in the negative graphite electrode can be localized for a current of up to 0.5C, but disappear for higher currents. After discharge, a fast internal voltage equalization was observed, leading to constant potential along the current collector within 12 min even though the relaxation process of the full cell is still ongoing. The measured internal battery parameters are used to verify multi-dimensional simulations and allow detailed analysis of further internal variables as current density and precise SOC distributions along the electrodes [32].
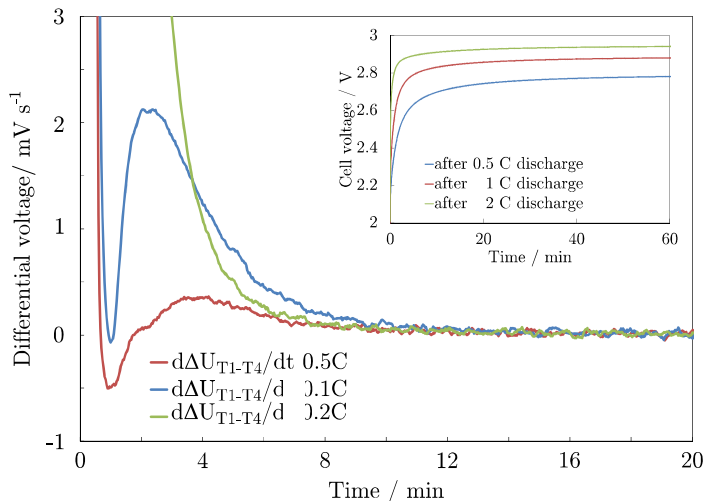
5. acknowledgement

Figure 13: Derivative in respect to time for the voltages differences ΔU_{T1-T4} for different discharge currents. Inlay: Voltage relaxation behavior at terminal T_1 for different discharge currents after reaching the 2 V cut-off voltage

[1] M. Armand, J.-M. Tarascon, Building better batteries, Nature 451 (7179) (2008) 652–657.

[2] J.-M. Tarascon, M. Armand, Issues and challenges facing rechargeable lithium batteries, Nature 414 (6861) (2001) 359–367.

[3] C. Pillot, Battery market development for consumer electronics, automotive and industrial: materials requirements and trends.

[4] M. Doyle, Modeling of galvanostatic charge and discharge of the lithium/polymer/insertion cell, Journal of The Electrochemical Society 140 (6) (1993) 1526.

[5] J. N. Reimers, Predicting current flow in spiral wound cell geometries, Journal of Power Sources 158 (1) (2006) 663–672.

[6] J. N. Reimers, Analytic theory for foil impedance in spiral wound cell geometries, Journal of Power Sources 262 (2014) 429–443.

[7] K.-J. Lee, K. Smith, A. Pesaran, G.-H. Kim, Three dimensional thermal-, electrical-, and electrochemical-coupled model for cylindrical wound large format lithium-ion batteries, Journal of Power Sources 241 (2013) 20–32.

[8] M. Guo, R. E. White, Mathematical model for a spirally-wound lithium-ion cell, Journal of Power Sources 250 (2014) 220–235.

[9] P. Taheri, A. Mansouri, M. Yazdanpour, M. Bahrami, Theoretical analysis of potential and current distributions in planar electrodes of lithium-ion batteries, Electrochimica Acta 133 (2014) 197–208.

[10] V. Zinth, C. von Lüders, M. Hofmann, J. Hattendorff, I. Buchberger, S. Erhard, J. Rebelo-Kornmeier, A. Jossen, R. Gilles, Lithium plating in lithium-ion batteries at sub-ambient temperatures investigated by in situ neutron diffraction, Journal of Power Sources 271 (2014) 152–159.

[11] P. Maire, A. Evans, H. Kaiser, W. Scheifele, P. Novak, Colorimetric determination of lithium content in electrodes of lithium-ion batteries, Journal of The Electrochemical Society 155 (11) (2008) A862.

[12] J. Liu, M. Kunz, K. Chen, N. Tamura, T. J. Richardson, Visualization of charge distribution in a lithium battery electrode, The Journal of Physical Chemistry Letters 1 (14) (2010) 2120–2123.

[13] J. Nanda, J. Remillard, A. O'Neill, D. Bernardi, T. Ro, K. E. Nietering, J.-Y. Go, T. J. Miller, Local state-of-charge mapping of lithium-ion battery electrodes, Advanced Functional Materials 21 (17) (2011) 3282–3290.

[14] A. Senyshyn, M. J. Mühlbauer, O. Dolotko, M. Hofmann, T. Pirling, H. Ehrenberg, Spatially resolved in operando neutron scattering studies on li-ion batteries, Journal of Power Sources 245 (2014) 678–683.

[15] K. Onda, T. Ohshima, M. Nakayama, K. Fukuda, T. Araki, Thermal behavior of small lithium-ion battery during rapid charge and discharge cycles, Journal of Power Sources 158 (1) (2006) 535–542.

[16] M. Fleckenstein, O. Bohlen, M. A. Roscher, B. Bäker, Current density and state of charge inhomogeneities in li-ion battery cells with lifepo4 as cathode material due to temperature gradients, Journal of Power Sources 196 (10) (2011) 4769–4778.

[17] T. Waldmann, M. Wohlfahrt-Mehrens, In-operando measurement of temperature gradients in cylindrical lithium-ion cells during high-current discharge, ECS Electrochemistry Letters 4 (1) (2014) A1–A3.

[18] G. Zhang, L. Cao, S. Ge, C.-Y. Wang, C. E. Shaffer, C. D. Rahn, In situ measurement of radial temperature distributions in cylindrical li-ion cells, Journal of the Electrochemical Society 161 (10) (2014) A1499–A1507.

[19] N. Martiny, J. Geder, Y. Wang, W. Kraus, A. Jossen, Development of a thin-film thermocouple matrix for in-situ temperature measurement in a lithium ion pouch cell, IEEE SENSORS 2013 - Proceedings 14 (10) (2013) 3377–3384.

[20] P. J. Osswald, M. D. Rosario, J. Garche, A. Jossen, H. E. Hoster, Fast and Accurate Measurement of Entropy Profiles of Commercial Lithium-Ion Cells, Electrochimica Acta (2015) 1–7.

[21] G. Zhang, C. E. Shaffer, C.-Y. Wang, C. D. Rahn, In-situ measurement of current distribution in a li-ion cell, Journal of the Electrochemical Society 160 (4) (2013) A610–A615.

[22] G. Zhang, C. E. Shaffer, C.-Y. Wang, C. D. Rahn, Effects of non-uniform current distribution on energy density of li-ion cells, Journal of the Electrochemical Society 160 (11) (2013) A2299–A2305.

[23] Y. F. Reynier, R. Yazami, B. Fultz, Thermodynamics of Lithium Intercalation into Graphites and Disordered Carbons, Journal of The Electrochemical Society 151 (3) (2004) A422.

[24] M. Tang, W. C. Carter, Y.-M. Chiang, Electrochemically driven phase transitions in insertion electrodes for lithium-ion batteries: Examples in lithium metal phosphate olivines, Annual Review of Materials Research 40 (1) (2010) 501–529.

[25] A. K. Padhi, K. S. Nanjundaswamy, G. J.B., Phospho-olivines as positiv-electrode materials for rechargeable lithium batteries, Journal of The Electrochemical Society 144 (4) (1997) 1188–1194.

[26] H. P. Boehm, R. Setton, E. Stumpp, Nomenclature and terminology of graphite intercalation compounds, Carbon (2) (1986) 241–245.

[27] J. R. Dahn, Phase Diagram of LixC6, Physical Review B 44 (17) (1991) 9170–9177.

[28] I. Bloom, J. P. Christophersen, D. P. Abraham, K. L. Gering, Differential voltage analyses of high-power lithium-ion cells, Journal of Power Sources 157 (1) (2006) 537–542.

[29] I. Bloom, A. N. Jansen, D. P. Abraham, J. Knuth, S. a. Jones, V. S. Battaglia, G. L. Henriksen, Differential voltage analyses of high-power, lithium-ion cells, Journal of Power Sources 139 (1-2) (2005) 295–303.

[30] I. Bloom, J. Christophersen, K. Gering, Differential voltage analyses of high-power lithium-ion cells, Journal of Power Sources 139 (1-2) (2005) 304–313.

[31] B. Wu, V. Yufit, M. Marinescu, G. J. Offer, R. F. Martinez-Botas, N. P. Brandon, Coupled thermal-electrochemical modelling of uneven heat generation in lithium-ion battery packs, Journal of Power Sources 243 (2013) 544–554.

[32] S. Erhard, P. J. Osswald, J. Wilhelm, A. Rheinfeld,

S. Kosch, A. Jossen, Simulation and measurement of local potentials within modied commercial cylindrical cells - part ii: Modeling approach and validation, Journal of the Electrochemical Society.